

## Improved Wind Measurements on Research Aircraft

D. KHELIF, S. P. BURNS, AND C. A. FRIEHE

*Department of Mechanical and Aerospace Engineering, University of California, Irvine, Irvine, California*

(Manuscript received 4 June 1998, in final form 14 October 1998)

### ABSTRACT

Improved techniques for measuring horizontal and vertical wind components and state variables on research aircraft are presented. They include a filtering method for correcting ground speed and position Inertial Navigation System data with Global Positioning System data, use of moist-air thermodynamic properties in the true airspeed calculation, postflight calculation of the aircraft vertical velocity, and calibration of airflow attack and sideslip angles from the two air-data systems on each aircraft—a radome gust probe and a pair of fuselage-mounted Rosemount 858Y probes. Winds from the two air-data systems are compared for the National Oceanic and Atmospheric Administration WP-3D aircraft.

As an evaluation of these techniques, data from the two aircraft during side-by-side low-level constant-heading runs are compared for mean and turbulent measurements of wind, ambient temperature, and absolute humidity. Small empirical offsets were determined and applied to the two latter scalars as well as to static and dynamic pressures. Median differences between mean horizontal wind components from nine comparisons were within  $0.1 \pm 0.4 \text{ m s}^{-1}$ . Median differences in latent heat and sensible heat fluxes and momentum flux components were  $3.5 \pm 15 \text{ W m}^{-2}$ ,  $0 \pm 2.5 \text{ W m}^{-2}$ , and  $0 \pm 0.015 \text{ Pa}$ , respectively.

### 1. Introduction

The past several decades have witnessed a large increase in the use of research aircraft to measure mean and turbulent winds and scalars such as temperature and humidity. Background on research aircraft measurements can be found in Lenschow (1986), Brown et al. (1983), Tjernstrom and Friehe (1991), and Bögel and Baumann (1991). Recent progress in navigation technology such as the Global Positioning System (GPS) and other technologies have led to new techniques and capabilities on research aircraft.

Some experiments place stringent accuracy requirements on the aircraft instrumentation such as the Tropical Ocean Global Atmosphere Coupled Ocean–Atmosphere Response Experiment (TOGA COARE) (Webster and Lukas 1992) in which predominant winds were very low (approximately  $2\text{--}4 \text{ m s}^{-1}$ ) and specific humidity very high (approximately  $18\text{--}20 \text{ g kg}^{-1}$ ). The purpose of this paper is to present the following improved techniques for wind measurements on research aircraft:

- GPS correction of Inertial Navigation System (INS) ground speed and position data,
- inclusion of moist-air thermodynamic properties in the calculation of true airspeed (especially important in the Tropics),
- calculation of aircraft vertical velocity by means of a filtering technique, and
- in situ calibration of slip and attack angles from radome and fuselage sensors.

Although these techniques were developed to process data from the two National Oceanic and Atmospheric Administration (NOAA) WP-3D Orion aircraft (N42RF and N43RF), they are also applicable to other aircraft.

Multiaircraft comparisons are useful to ensure measurement quality (LeMone and Pennell 1980; MacPherson et al. 1992) and to facilitate comparison of similar instrumentation between two (or more) aircraft (Lenschow et al. 1991). As a data quality check, mean and turbulent measurements of ambient temperature, specific humidity, and earth-based winds by the two WP-3Ds from wingtip-to-wingtip comparison time periods during TOGA COARE are used. Eddy correlation fluxes of latent and sensible heat and momentum were also compared.

### 2. Instrumentation and data system

The main instrumentation (identical on both WP-3Ds) is shown in Fig. 1 and summarized in Table 1. Many

---

*Corresponding author address:* Dr. Djamal Khelif, Department of Mechanical and Aerospace Engineering, University of California, Irvine, Irvine, CA 92697-3975.  
E-mail: dkhelif@uci.edu

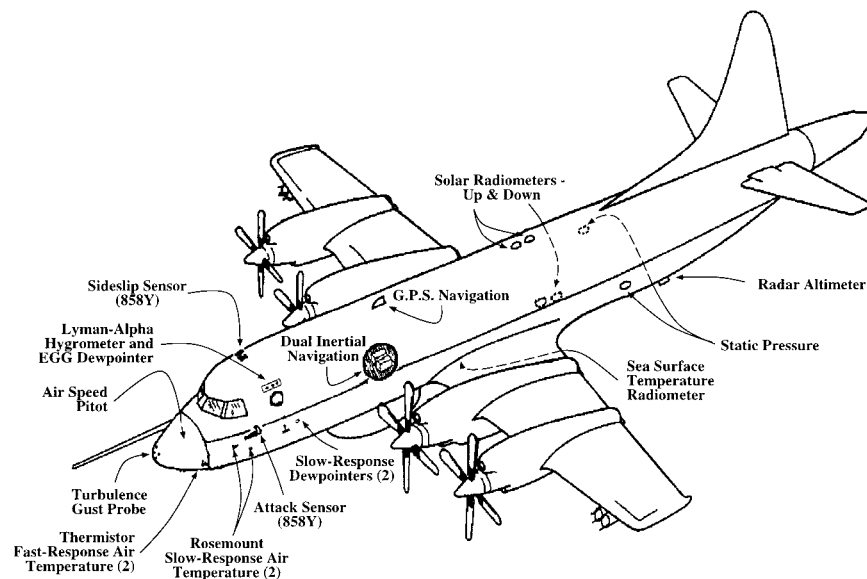


FIG. 1. Sketch of NOAA WP-3D instrumentation.

variables are measured redundantly in order to enhance data integrity. The velocity vector of the air with respect to the aircraft, for example, is measured by two independent systems: a five-pressure-port radome system (Brown et al. 1983) and two Rosemount 858Y probes combined with a fuselage-mounted pitot tube. Antialiasing filters were applied to analog data that were then digitized with 14-bit resolution and recorded at 1 Hz continuously and at 40 Hz for selected periods of time for subsequent flux and spectral calculations. More information on the data acquisition system and sensor calibrations can be obtained from the NOAA Aircraft Operations Center (AOC).<sup>1</sup>

### 3. State parameters

#### a. Temperature

Aircraft temperature sensors measure recovery temperatures, which have to be corrected to total temperatures with a known recovery factor for the particular temperature probe (Rosemount 1981). Calculation of ambient temperature is obtained using the compressible flow equation (Liepmann and Roshko 1967). Dynamic pressure is required in the calculation of ambient temperature, and on the WP-3Ds, the frequency response of the pressure transducers is about 10 times that of the slow-response temperature sensor–amplifier system (about 1 Hz for the copilot’s fuselage Pitot and 0.1 Hz for the Rosemount 102a deiced temperature probe). To

exclude the erroneous high-frequency content above 0.1 Hz in the calculated ambient temperature from the Rosemount 102a sensors, the dynamic pressure signal was matched to that of the total temperature by low-pass filtering it to 0.1 Hz with a Butterworth zero-phase shift digital filter.

Differences between measurements from the four Rosemount 102a temperatures on the WP-3Ds (see Table 1) ranged over approximately 0.4°C. These were found to be systematic errors as revealed by extensive aircraft–aircraft intercomparisons involving five TOGA COARE aircraft and were corrected by applying constant empirical offsets. On each WP-3D, one of these sensors was chosen as the “reference” sensor and used for all calculations involving ambient temperature. The values of the offsets applied to data from the two chosen sensors are given in Table 2.

For turbulence and flux measurements, data from redundant experimental fast-response sensors [two ~130  $\mu\text{m}$  diameter thermistor beads in a Rosemount 102E4AL housing, similar to the single bead probe described by Friehe and Khelif (1992) and analyzed by Fuehrer et al. (1994)] were used. Response to several hertz is expected from these sensors.

Thermodynamic properties of dry air were used in the compressible flow equation [Eq. (A23)] for both types of temperature sensors to calculate ambient temperature. (Tests using moist-air properties revealed insignificant differences in ambient temperatures compared to using dry-air properties, so the latter were used for simplicity and to avoid introducing possible spikes and noise from humidity signals.)

In contrast to the common practice of using a constant

<sup>1</sup> NOAA AOC, P.O. Box 6829, MacDill Air Force Base, FL 33608-0829.

TABLE 1. NOAA WP-3D aircraft instrumentation and measured parameters.

Parameter	Instrument <sup>a</sup>	Location <sup>b</sup>	Accuracy	Resolution	F/S <sup>c</sup>	
Position	Northrop/Delco Carousel-IV INS (2)	Cabin	1500 m	10 m		
	Trimble 2100 GPS <sup>d</sup>	Cabin	100 m	9.1 m		
Ground-speed vector	Northrop/Delco Carousel-IV INS (2)	Cabin	$\pm 1.5 \text{ m s}^{-1}$	$0.00019 \text{ m s}^{-1}$		
	Trimble 2100 GPS <sup>d</sup>	Cabin	$0.05 \text{ m s}^{-1}$	$0.0002 \text{ m s}^{-1}$		
Attitude angles						
Heading	Delco Carousel-IV INS (2)	Cabin	$\pm 0.1^\circ$	$6.1 \times 10^{-50}$		
pitch, roll	Delco Carousel-IV INS (2)	Cabin	$\pm 0.06^\circ$	$8.6 \times 10^{-50}$		
Aircraft altitude	Stewart-Warner APN-159 Radar Alt.	Belly	$\pm 1\%$	1 m	S	
	Gould APN-232 Radar Altimeter	Belly	$\pm 2\%$	1 m	S	
Humidity						
Chilled mirror hygrometers	AOC-modified General Eastern Sensor	Fuselage, P	$\pm 0.5^\circ\text{C}$	$0.0028^\circ\text{C}$	S	
	General Eastern Model 1011	Fuselage, P	$\pm 0.5^\circ\text{C}$	$0.0033^\circ\text{C}$	S	
	EG&G Model 137-C3	Fuselage, P	$\pm 0.5^\circ\text{C}$	$0.0062^\circ\text{C}$	S	
Water vapor absorption	Lyman- $\alpha$ hygrometer	Fuselage, P	In situ	Calibration	F	
	NCAR UV hygrometer <sup>e</sup>	Fuselage, P			F	
Recovery temperature						
Platinum wire sensors	Deiced Rosemount 102 housing configuration "a," (2)	Fuselage P(2)	$\pm 0.6^\circ\text{C}$	$0.004^\circ\text{C}$	S	
	nondeiced Rosemount 102E4AL housing, 25- $\mu\text{m}$ wire, <sup>e</sup>	Radome P	$\pm 0.4^\circ\text{C}$		F	
Thermistor sensors	Nondeiced Rosemount 102E4AL housing, 127- $\mu\text{m}$ thermistor bead (2)	Radome, P(2)	In situ	Calibration	F	
Airspeed vector						
$\Delta P_\alpha$	Differential attack pressure	Rosemount 858Y five-hole probe	Fuselage, P		F	
		Rosemount 1221F2VL transducer		$\pm 0.22 \text{ hPa}$	$0.002 \text{ hPa}$	
		Flush radome pressure ports	Radome			F
$\Delta P_\beta$	Differential sideslip pressure	Rosemount 1221F1VL transducer		$\pm 0.19 \text{ hPa}$	$0.002 \text{ hPa}$	
		Rosemount 858Y five-hole probe	Fuselage, Top			F
		Rosemount 1221F2VL transducer		$\pm 0.22 \text{ hPa}$	$0.002 \text{ hPa}$	
"pseudo" dynamic pressure	"Pseudo" dynamic pressure	Flush radome pressure ports	Radome		F	
		Rosemount 1221F1VL transducer		$\pm 0.19 \text{ hPa}$	$0.002 \text{ hPa}$	
		Rosemount 858Y five-hole probe	Fuselage, P			F
$P_{qm}$	"True" dynamic pressure	Rosemount 1221F2AF transducer		$\pm 0.55 \text{ hPa}$	$0.005 \text{ hPa}$	
		Rosemount 858Y five-hole probe	Fuselage, Top			F
		Rosemount 1221F2VL transducer		$\pm 0.55 \text{ hPa}$	$0.005 \text{ hPa}$	
		Pitot tube	Wing			F
		Rosemount 1281AF transducer		$\pm 0.53 \text{ hPa}$	$0.005 \text{ hPa}$	
		Pitot tube	Fuselage, St			F
Static pressure	Flush pressure ports	Rosemount 1281AF transducer		$\pm 0.53 \text{ hPa}$	$0.005 \text{ hPa}$	
		Rosemount 1221F1AF transducer		$\pm 1.1 \text{ hPa}$	$0.01 \text{ hPa}$	
		Flush radome pressure port	Radome			F
		Rosemount 1221F1AF transducer		$\pm 1.1 \text{ hPa}$	$0.01 \text{ hPa}$	
			$\pm 1.6 \text{ hPa}$	$0.02 \text{ hPa}$		

<sup>a</sup> INS: Inertial Navigation System, GPS: Global Positioning System.

<sup>b</sup> P: Port Side, St: Starboard Side.

<sup>c</sup> F: Fast-response sensor, S: Slow-response sensor.

<sup>d</sup> 95% of the time more accurate than values shown [degraded because of selective availability (S/A)].

<sup>e</sup> Inoperative for most TOGA COARE flights.

recovery factor for temperature probes, the Mach number-dependent correction function  $\eta$  was used as described by Rosemount (1981):

$$\eta = \frac{T_t - T_r}{T_t}, \quad (1)$$

where  $T_t$  and  $T_r$  are the total and recovery temperatures in kelvins, respectively. The recovery factor  $R_f$  is related to  $\eta$  by

$$R_f = 1 - \eta \left[ 1 + \frac{2}{(\gamma - 1)M^2} \right], \quad (2)$$

where  $M$  is the dry-air Mach number and  $\gamma$  is the specific heat ratio of dry air. Curves showing the variations of  $\eta$  versus  $M$  obtained from wind tunnel tests were given by Rosemount (1981) for each of the two types of probes used in this study. These were digitized and least squares fit for the operating range of the WP-3D aircraft ( $0.3 < M < 0.5$ ). The error in ambient temperature was up

TABLE 2. Empirical offsets added to ambient temperature, dewpoint temperature, static pressure, fuselage dynamic pressure ( $P_{qf1}$ ), and radome dynamic pressure ( $P_{qr}$ ) measurements on the WP-3D aircraft ( $T_d$  empirical offset on N42RF was flight to flight dependent), and fuselage attack and sideslip angles calibration coefficients.

Aircraft	Empirical offsets					Calibration coefficient			
	$T_a$ (°C)	$T_d$ (°C)	$P_s$ (hPa)	$P_{qf1}$ (hPa)	$P_{qr}$ (hPa)	$S_\alpha$ (°)	$I_\alpha$ (°)	$S_\beta$ (°)	$I_\beta$ (°)
N42RF	0	-0.35 <sup>a</sup> -0.50 <sup>b</sup> -0.45 <sup>c</sup>	-0.1	1.30	1.20	5.94	2.16	5.67	0.35
N43RF	-0.15	0.00	0.3	1.25	0.80	6.17	1.07	5.60	-0.05

<sup>a</sup> 921113 and 921126.

<sup>b</sup> 921128.

<sup>c</sup> 930109.

to 0.1°C when the Mach number dependence of  $R_f$  was not taken into account. Since  $\eta$  increases with  $M$ , this error will be more significant for faster aircraft.

### b. Humidity

Each WP-3D was equipped with three slow-response chilled-mirror-type dewpoint sensors (see Table 1). (Data from the EG&G dewpoint sensor on N42RF were ignored since they were 5°C larger than those from the AOC and General Eastern sensors.) The AOC sensor (which did not work on flights before 921128<sup>2</sup>) measured slightly higher dewpoints (by ~0.2°C) than the General Eastern sensor. For N43RF, the three sensors were generally within approximately ±0.2°C of each other. Examination of data from aircraft-aircraft comparison legs revealed that dewpoints on N42RF were ~0.5°C greater than those on N43RF. Based on comparisons with other TOGA COARE aircraft and surface platforms, it was decided to decrease the N42RF General Eastern by 0.5°C (see Table 2).

For turbulence measurements and flux calculations, each WP-3D was outfitted with a fast-response Lyman- $\alpha$  humidimeter. Its log amplifier output voltage was linearly least squares fit to absolute humidity obtained from the General Eastern dewpoint signal. Approximately 4 h of 1-Hz data in the middle portion of a boundary layer flight (where the dewpoint temperatures were above 0°C) were typically used in the calibration. Friehe et al. (1986) found that accounting for the time lag of 2 s in an EG&G dewpoint instrument improved Lyman- $\alpha$  least squares fit for short data segments. In a similar way, the General Eastern dewpoint was found to lag the Lyman- $\alpha$  by nearly 2 s, and therefore, its signal was advanced by 2 s, resulting in an improved fit of the Lyman- $\alpha$  calibration.

### c. Static pressure defect

Static pressure is normally measured from the aircraft manufacturer's fuselage static ports or from the static side of Pitot-static probes. Since the flow around the aircraft alters the static pressure field, determination of the difference between the true static pressure away from the aircraft in the same horizontal plane  $P_s$  and that measured  $P_{sm}$  is required. This is called the static pressure defect  $P_{sd}$  or "position error" (Brown 1988). For the WP-3Ds this was determined over a range of airspeeds at different altitudes for the fuselage static pressure ports using the "trailing-cone" system, in which a semirigid tube with a static port is trailed far behind the aircraft in the undisturbed air. Measurements of  $P_{sd}$  were in the range 0.02–0.7 hPa and were fitted to the expression:

$$P_{sd} = P_{sm} - P_{sc} \\ = c_4(P_{qm}^3) + c_3(P_{qm}^{2.5}) + c_2(P_{qm}^2) + c_1(P_{qm}), \quad (3)$$

where  $P_{qm}$  is the measured dynamic pressure,  $P_{sc}$  is the corrected static pressure, and  $c_1$ – $c_4$  are empirical constants. The constants were found to differ slightly between the two aircraft. Aircraft-to-aircraft comparisons during TOGA COARE revealed that  $P_{sm}$  between N42RF and N43RF were in closer agreement than the  $P_{sc}$  data by ~0.25 hPa. This indicates that the correction on one, or both, of the aircraft may have a small error. To correct for this difference,  $P_{sc}$  data from the National Center for Atmospheric Research (NCAR) Electra were compared, and empirical  $P_{sc}$  offsets of -0.1 hPa (N42RF) and +0.3 hPa (N43RF) were used. It should be noted that  $P_{sd}$  was small for nominal cruise conditions in the boundary layer.

## 4. Horizontal wind measurements

The principles of wind measurement from aircraft are given by Axford (1968) and summarized by Lenschow (1986). The horizontal wind vector components  $u$  and  $v$  in the geographic coordinate system ( $x$  positive eastward,  $y$  positive northward, and  $z$  positive upward) are

<sup>2</sup> Nomenclature used to identify a specific TOGA COARE flight is the UTC year, month, and day of the mission takeoff date in the form of a six-digit number. For example, 921128 refers to the flight whose takeoff was on UTC 28 November 1992.

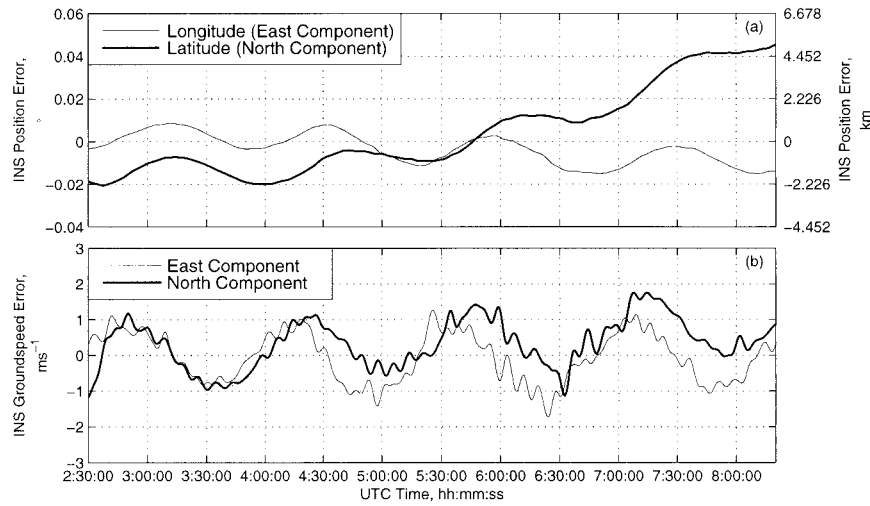


FIG. 2. INS correction signal to (a) position and (b) aircraft ground-speed velocity components.

$$\begin{aligned}
 u &= u_p - U_a D \\
 &\times [\sin\psi \cos\theta + \tan\beta(\cos\psi \cos\phi + \sin\psi \sin\theta \sin\phi) \\
 &\quad + \tan\alpha(\sin\psi \sin\theta \cos\phi - \cos\psi \sin\phi)] \\
 &\quad - L(\dot{\theta} \sin\theta \sin\psi - \dot{\psi} \cos\psi \cos\theta)
 \end{aligned} \quad (4)$$

$$\begin{aligned}
 v &= v_p - U_a D \\
 &\times [\cos\psi \cos\theta - \tan\beta(\sin\psi \cos\phi - \cos\psi \sin\theta \sin\phi) \\
 &\quad + \tan\alpha(\cos\psi \sin\theta \cos\phi + \sin\psi \sin\phi)] \\
 &\quad - L(\dot{\psi} \sin\psi \cos\theta + \dot{\theta} \cos\psi \sin\theta),
 \end{aligned} \quad (5)$$

where  $u_p$  and  $v_p$  are the east and north aircraft velocity components, respectively;  $U_a$  is the true airspeed;  $\alpha$ ,  $\beta$ ,  $\theta$ ,  $\phi$ , and  $\psi$  are the aircraft attack, sideslip, pitch, roll, and true heading angles, respectively;  $L$  is the distance separating the INS and gust probe along the aircraft's center line;  $D = (1 + \tan^2\alpha + \tan^2\beta)^{-1/2}$ ; and  $\dot{\psi} = d\psi/dt$  and  $\dot{\theta} = d\theta/dt$ . Since the WP-3D aircraft do not respond to motion with frequencies above  $\sim 1$  Hz, the 40-Hz INS angle data ( $\theta$ ,  $\phi$ , and  $\psi$ ) were low-pass filtered at a cutoff frequency of 1 Hz with a Butterworth zero-phase shift digital filter that effectively excluded the high-frequency noise.

Errors in any of the measured quantities in the above equations will cause errors in the wind components; Tjernstrom and Friehe (1991) identified the limited resolutions and accuracies of heading and ground speed components from the INS as the major factors limiting the accuracy of the horizontal wind. In TOGA COARE, the nominal boundary layer state was very low winds (approximately  $1\text{--}4 \text{ m s}^{-1}$ ) with high dewpoint temperature (approximately  $23^\circ\text{--}24^\circ\text{C}$ ), which place stringent requirements on the aircraft wind measurements. In particular, INS drift and Schuler oscillation have to be accounted for, and as will be shown, thermodynamic properties for moist air have to be used in the com-

pressible flow equations for true airspeed to obtain accurate winds in these conditions.

#### a. Postflight GPS correction of INS data

Methods to correct INS data for drift and the Schuler oscillation have been presented by Leach and MacPherson (1994, 1991), Masters and Leise (1993), and Matejka and Lewis (1997). Leach and MacPherson used a Kalman filtering technique to model the INS errors; Masters and Leise used differences between Loran C and INS in the correction; and Matejka and Lewis incorporated INS and GPS information in a variational solution. For the WP-3Ds, we chose the simpler approach of using the differences between the GPS and INS data, suitably processed, for ground speed and position corrections.

To produce accurate INS-GPS blended data, differences between the GPS and INS data were low-pass filtered at 0.0025 Hz ( $\sim 6.7$ -min period) to form a correction signal that was then added to the raw INS data. This cutoff frequency was chosen to correct for both the Schuler oscillation ( $\sim 84$ -min period) and higher-frequency ( $\sim 8$ -min period) errors in the INS data. The high-frequency INS errors (see Fig. 2) are qualitatively consistent with those found by Leach and MacPherson (1994). The correction method used also eliminates higher-frequency fluctuations of the GPS data that are unrealistic (perhaps due to GPS selective availability). Results of the correction scheme for a typical flight (Fig. 2) show that ground speed errors due to Schuler oscillation (approximately  $\pm 1 \text{ m s}^{-1}$ ) and those associated with higher-frequency oscillations (approximately  $\pm 0.5 \text{ m s}^{-1}$ ) are both accounted for.

#### b. Airspeed equations

Although the use of thermodynamic properties for moist air did not affect the calculation of ambient tem-

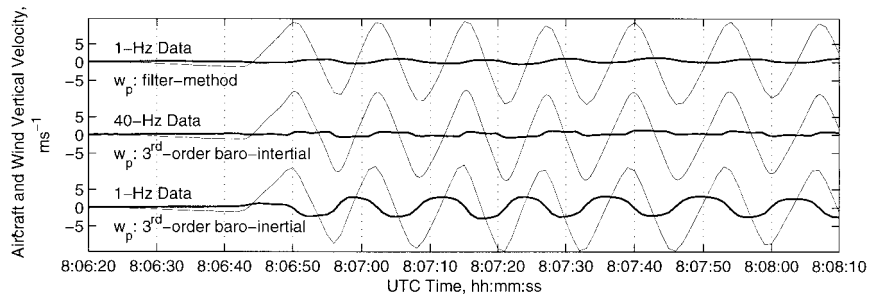


FIG. 3. A pitching maneuver comparing the aircraft vertical velocity ( $w_p$ , thin line) and the calculated vertical wind ( $w$ , thick line). Data sampling rate and the method of  $w_p$  calculation are indicated.

perature, it is necessary to account for humidity effects on true airspeed for TOGA COARE boundary layer conditions. Lenschow (1986) presented results obtained by C. Friehe that showed true airspeed errors of 1%–2% for dewpoint temperatures of 20°–30°C. Since the WP-3Ds fly at  $\sim 100 \text{ m s}^{-1}$ , errors in horizontal winds would be 1–2  $\text{m s}^{-1}$  because of this effect alone. That early analysis of moist-air thermodynamic properties was found to be in error. A correct derivation is presented in the appendix. For a dewpoint temperature of 24°C for sea level, the WP-3Ds true airspeed is found to increase by  $\sim 0.6 \text{ m s}^{-1}$  from that calculated with dry-air thermodynamic properties, which is significant for tropical conditions.

The dynamic pressure is another possible source of error in true airspeed measurements (and other measurements such as ambient temperature and airflow angles). In addition to the laboratory calibration of the pressure transducers, reverse heading maneuvers were used to determine empirical biases in the radome and fuselage dynamic pressures. These offsets were obtained by minimizing the difference in the longitudinal wind component (in aircraft coordinates) between the two legs of the maneuver and are shown in Table 2. The offsets were determined independently for each sensor and aircraft.

*c. Sideslip calibration*

The calibration of the radome and fuselage sideslip differential pressures  $\Delta P_\beta$  to obtain sideslip angle  $\beta$  was performed on data from reverse heading maneuvers using the first-order relationship

$$\beta = S_\beta \frac{\Delta P_\beta}{P_{qc}} + I_\beta, \tag{6}$$

where  $P_{qc}$  is the corrected dynamic pressure (radome or fuselage),  $S_\beta$  the sensitivity, and  $I_\beta$  the offset. Since the horizontal wind field is assumed stationary during the time of the maneuver,  $S_\beta$  and  $I_\beta$  were determined by means of an iterative method in which the differences in the earth-based wind components  $u$  and  $v$  before and after the turn were minimized. The  $S_\beta$  and  $I_\beta$  values

found for the Rosemount 858Y probe are given in Table 2. Unlike the method usually used of minimizing differences in the aircraft-based lateral wind, this technique allows for departures by a few degrees from an 180° difference between initial and reciprocal legs.

**5. Vertical wind measurements**

The vertical wind vector component  $w$  is given by Lenschow (1986) as

$$w = w_p - U_a D [\sin\theta - \tan\beta \cos\theta \sin\phi - \tan\alpha \cos\theta \cos\phi] + L\dot{\theta} \cos\theta, \tag{7}$$

where  $w_p$  is the aircraft vertical velocity, and all other parameters are defined as in Eqs. (4) and (5). This section describes the calculation technique for  $w_p$  and calibration of the angle of attack,  $\alpha$ .

*a. Aircraft vertical velocity*

It is well known that the real-time integration of the INS vertical acceleration diverges and the aircraft vertical velocity  $w_p$  should be recalculated in postflight processing with a stable reference parameter to limit the error growth (Lenschow and Spyers-Duran 1989). The “third-order baro-inertial loop” method (Blanchard 1971) integrates the INS vertical acceleration while keeping errors small, and it typically uses the barometric pressure altitude as the reference. This method was adapted for the postflight recalculation of  $w_p$  using the three constants determined by Lenschow and Spyers-Duran (1989), which results in a 60-s time constant for the correction algorithm, but as will be shown, it was not possible to use this algorithm for the 1-Hz data.

When the baro-inertial loop  $w_p$  was used to calculate  $w$ , the 1- and 40-Hz  $w$  data were significantly different. An example of this difference during a typical pitching maneuver is shown in Fig. 3. The 1-Hz data are the bottom time series, and the 40-Hz data are in the center. Spectral analysis revealed that a 60-s time constant in the third-order baro-inertial loop resulted in a time advance,  $\Delta t \approx 0.5(1/\text{sample rate})$ , in the recalculated  $w_p$  output. Therefore, this method worked well for the 40-

Hz data, where the introduced  $\Delta t$  in the recalculated  $w_p$  was too small (0.0125 s) to have a significant effect on the  $w$  calculation but failed for the 1-Hz data that were severely affected by the introduction of a 0.5-s time advance.

To overcome the discrepancy between the 1- and 40-Hz  $w_p$  data, a new technique was used to calculate the slow-rate  $w_p$  without introducing any time shift. The technique blends together two sources of velocity measurements—one accurate at high frequencies and the other accurate at low frequencies—that were combined after their respective inaccurate portions were filtered out digitally. The accurate high-frequency data were obtained by linearly detrending the numerically integrated INS vertical acceleration output and then applying a four-pole Butterworth zero-phase-shift high-pass filter. The low-frequency portion of the  $w_p$  data was calculated by taking the time-derivative of barometric pressure altitude, and then a four-pole Butterworth zero-phase-shift low-pass filter was used to attenuate the high-frequency noisy portion of the signal. The resulting filtered signals were added to create the final 1-Hz recalculated  $w_p$  data. For both the low-pass and high-pass filters a 0.03-Hz ( $\sim 33.3$  s) cutoff frequency was used. This value was determined by iteration of cutoff frequency over the range 0.001–0.5 Hz and comparing level-run statistics (mean and variance) of  $w_p$  for several different flights. Between 0.01 and 0.03 Hz, these statistics were relatively insensitive to changes in cutoff frequency and therefore, the 0.03 Hz value was used. It should be noted that any precise altitude measurement can be used with this technique. Because of the coarse resolution of the WP-3D radar altimeters ( $\sim 1$  m), the pressure altitude data were used instead. The 1-Hz vertical wind calculated with  $w_p$  from the filter method is shown in the upper time series of Fig. 3 and does not show the modulations that are present in  $w$  when  $w_p$  is determined with the baro-inertial loop method (lower time series in Fig. 3).

### b. Vertical maneuvers

The radome gust probe sensor and the fuselage-mounted Rosemount model 858Y flow angle sensor provide two independent measurements of attack angle. The differential attack pressure from each sensor  $\Delta P_\alpha$  was calibrated to obtain angle of attack  $\alpha$  using in-flight data and assuming a linear relationship of the form

$$\alpha = S_\alpha \frac{\Delta P_\alpha}{P_{qc}} + I_\alpha, \quad (8)$$

where  $S_\alpha$  and  $I_\alpha$  are sensitivity and offset of  $\alpha$  and  $P_{qc}$ , the corrected dynamic pressure. Measurements of  $P_{qc}$  from a fuselage-mounted Pitot tube sensor and from the radome center hole were used for the calibration of fuselage and radome, respectively.

Previous calibration methods for attack angle have typically used maneuvers in quiescent air at high alti-

tudes so that  $w = 0$  could be assumed to determine  $S_\alpha$  and  $I_\alpha$  (Brown et al. 1983; Tjernstrom and Friehe 1991; Friehe et al. 1996), or else had specially designed booms that allowed for the probe angle to be altered (Wood et al. 1997). Calibration quality is often evaluated by comparing variations in  $w$  with  $w_p$  during “pitching” maneuvers where  $w_p$  is varied purposefully. The rule-of-thumb criterion for acceptable vertical winds is when the “peak-to-peak” variations of  $w$  are less than 10% of the variations of  $w_p$  during pitching (Lenschow 1986). These maneuvers are also instrumental in detecting possible phase differences between the different terms in Eq. (7) (Bögel and Baumann 1991; Tjernstrom and Samuelsson 1995). However, a drawback of pitching maneuvers is that they are performed at high altitude (for safety and to avoid turbulent “noise”) and thus could yield calibration coefficients that are not suitable for the denser air and different aircraft trim conditions that are typical of level runs in the boundary layer.

An alternative in situ technique was developed to calibrate  $\alpha$  from straight and level runs in the boundary layer. The technique is also applied to a set of pitching maneuver data for comparison. In this new approach,  $S_\alpha$  and  $I_\alpha$  were determined by iterating  $S_\alpha$  and  $I_\alpha$  and then examining the mean and variance of the resulting vertical wind. Contours of the mean and variance of  $w$  are shown as a function of  $S_\alpha$  and  $I_\alpha$  in Fig. 4 for both a pitching maneuver and a low-level run. From these results it can be observed that as expected the mean of  $w$  depends mostly on  $I_\alpha$ , while its variance depends mostly on  $S_\alpha$ . To find a pair of coefficients ( $S_\alpha, I_\alpha$ ) that would apply to all TOGA COARE flights, a 1-Hz dataset consisting of seven pitching maneuvers and another of 80 low-level runs (50–120 km long) from seven different flights were used to calculate two sets of contours (similar to those in Fig. 4). On each of the two datasets, the iteration method uses an optimization algorithm with two constraints: (i) the overall mean of  $w$  is forced to be as close to zero as possible, and (ii) the overall variance of  $w$  is minimized. While the first constraint is straightforward, the second stems from the assumption that for a large dataset, if a value of  $S_\alpha$  other than the correct one for the given gust probe is used in Eq. (8), the calculated overall variance of  $w$  would be larger than the actual variance of  $w$ . In practice,  $S_\alpha$  and  $I_\alpha$  are weakly interdependent, and the method yields the optimal pair ( $S_\alpha, I_\alpha$ ) that best satisfies the two constraints above. In Fig. 4 the N43RF optimal values are indicated by a “P” for the pitching maneuver dataset values ( $S_{\alpha,P}, I_{\alpha,P}$ ) and an “R” for the level-run dataset values ( $S_{\alpha,R}, I_{\alpha,R}$ ). Differences between  $S_{\alpha,P}$  and  $S_{\alpha,R}$  were  $\sim 5\%$  for N42RF and  $\sim 11\%$  for N43RF.

To choose between the ( $S_\alpha, I_\alpha$ )<sub>P</sub> and ( $S_\alpha, I_\alpha$ )<sub>R</sub> values, the mean vertical wind from low-level constant-heading legs were considered. As shown in Fig. 5, the leg-long means of  $w$  calculated with  $\alpha$  from pitching maneuver coefficients ( $S_\alpha, I_\alpha$ )<sub>P</sub> ranged consistently from  $-0.4$  to  $-0.2$  m s<sup>-1</sup>. In addition to these unrealistic mean values,

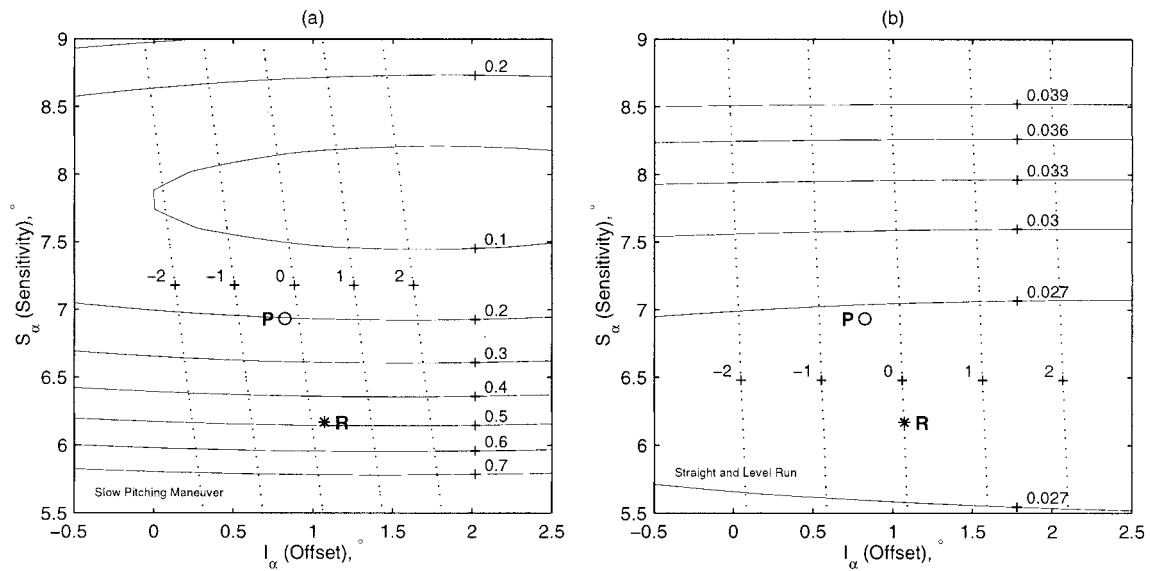


FIG. 4. Contours of mean (dotted,  $m\ s^{-1}$ ) and variance (solid,  $m^2\ s^{-2}$ ) of the 1-Hz calculated vertical wind velocity  $w$  while varying the sensitivity ( $S_\alpha$ ) and offset ( $I_\alpha$ ) of the angle of attack equation. Data are from the N43RF fuselage sensor from 921128 during (a) a pitching maneuver and (b) a low-level run. (See text for a description of the points “R” and “P.”)

the N43RF  $w$  data had a dependence on the aircraft pitch angle  $\theta$  (e.g., Fig. 5, N43RF on 921216). In contrast to this, when the low-level run coefficients ( $S_\alpha, I_\alpha$ )<sub>R</sub> were used, the leg-long means of  $w$  were near zero (as a result of the first constraint in the calibration) and there was no dependence on  $\theta$ . Also, the  $S_{\alpha,R}$  values between N42RF and N43RF agreed well ( $\sim 3\%$ ), which was expected since the sensors are both Rosemount 858Y probes and mounted in the same location on their respective aircraft. As shown in Fig. 9f, these values lead to a reasonable agreement in the standard deviation of  $w$  between the WP-3Ds. Values of  $I_{\alpha,R}$  between the aircraft differed by more than 50% (perhaps due to dif-

ferences in the sensor alignment relative to the airstream), but more importantly, the leg-long  $w$  means for each aircraft were near zero. For these reasons, the coefficients used in the data processing were the ( $S_\alpha, I_\alpha$ )<sub>R</sub> values shown in Table 2. The trade-off in using the low-level ( $S_\alpha, I_\alpha$ )<sub>R</sub> values was that the high-altitude pitching maneuver data were not optimal for N43RF, where results from the pitching maneuver quality evaluation were, on average, slightly higher than the maximum 10% rule. For N42RF, the pitching maneuvers generally met the maximum 10% criterion. An example with both 1- and 40-Hz data is shown in Fig. 3.

Whereas the above method was found to give con-

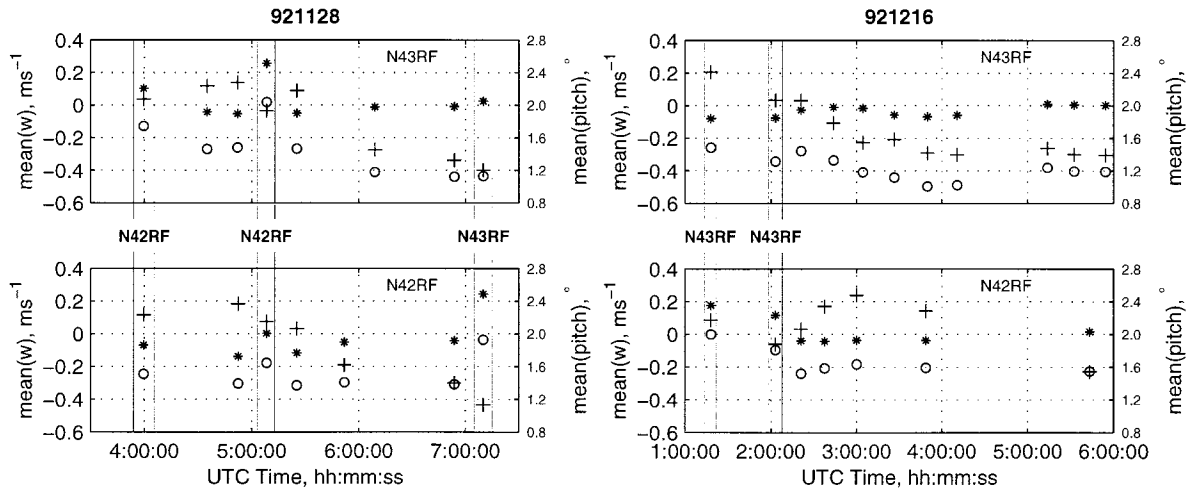


FIG. 5. Low-level entire-leg means of pitch angle (+) and vertical wind  $w$  calculated using optimal ( $S_\alpha, I_\alpha$ ) coefficients from low-level runs (\*) and from pitching maneuvers (O) data. Results are from (bottom) N42RF and (top) N43RF during the (left) 921128 and (right) 921216 missions. Vertical lines indicate intercomparison periods with the lead aircraft indicated by the middle text.

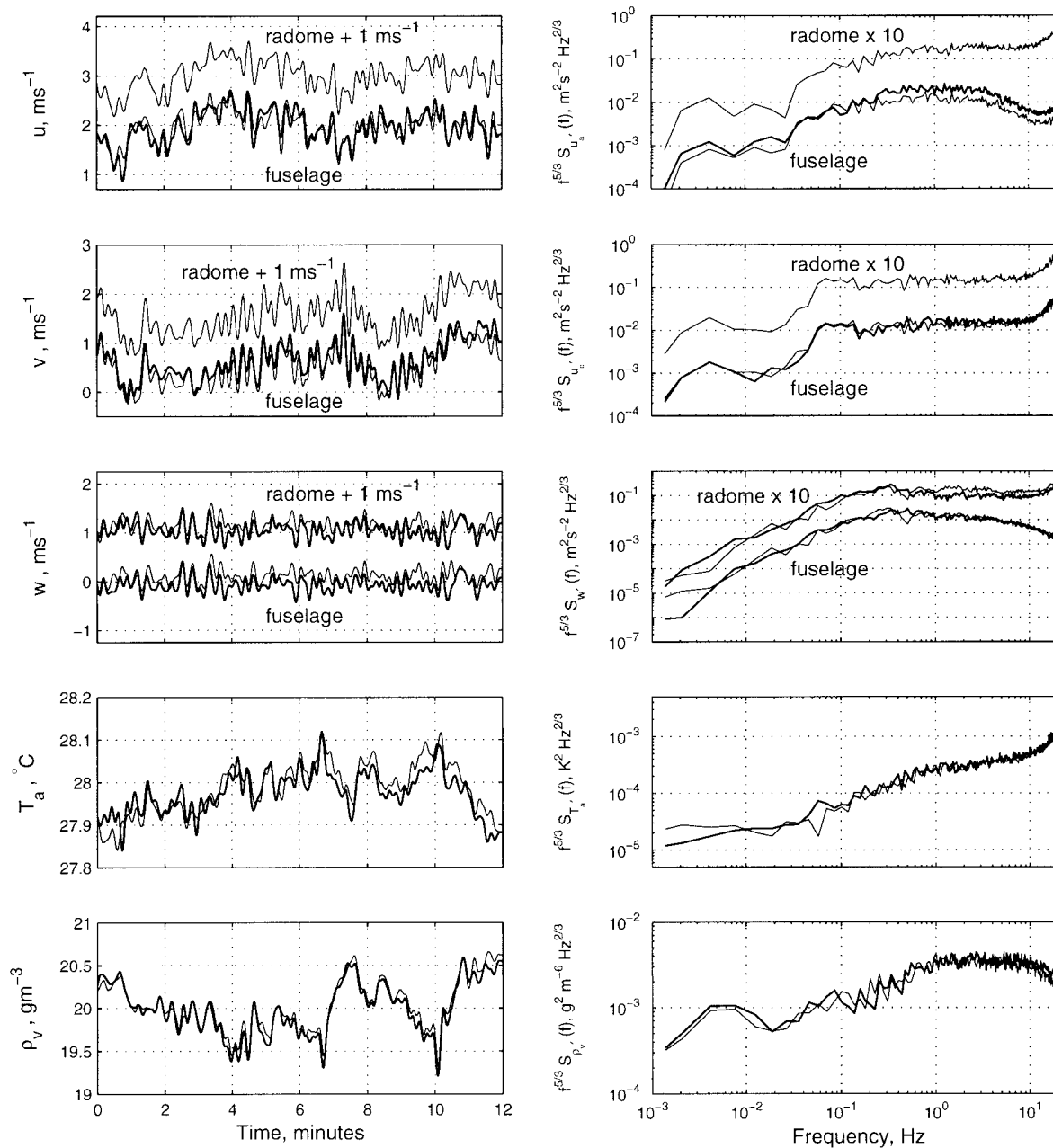


FIG. 6. Filtered high-rate (40 Hz) time series (left) and power spectra (right) of (from top to bottom) east, north, and vertical wind components (power spectra of along-wind and crosswind components are shown); temperature, and absolute humidity for N42RF (thick line) and N43RF (thin line). Both fuselage (Rosemount 858Y) and radome gust probes measurements are shown. Data from the latter were offset deliberately by the amount indicated on each plot for clarity. (The horizontal wind data on the N42RF radome were flawed because of leaks in the pressure lines; therefore, they are not shown.)

sistent results for the fuselage sensor data, applying it to the radome data led to the conclusion that the radome calibrations were variable throughout TOGA COARE. Further investigation revealed that on certain flights there were inconsistencies in  $\Delta P_a$  data from the radome when compared to the fuselage data and were attributed to leaks in the radome system.

Another observation, highlighted by the vertical lines

in Fig. 5, is that, when the two WP-3Ds were flying in close formation, the mean  $w$  of the trailing aircraft was increased by  $\sim 0.2 \text{ m s}^{-1}$ . The cause of this may have been the trailing vortex of the leading aircraft disturbing the airflow around the following aircraft, or possibly the trailing aircraft was trimmed differently than in free flight and was subject to pilot-induced maneuvering to maintain formation. In either case, the flow near the

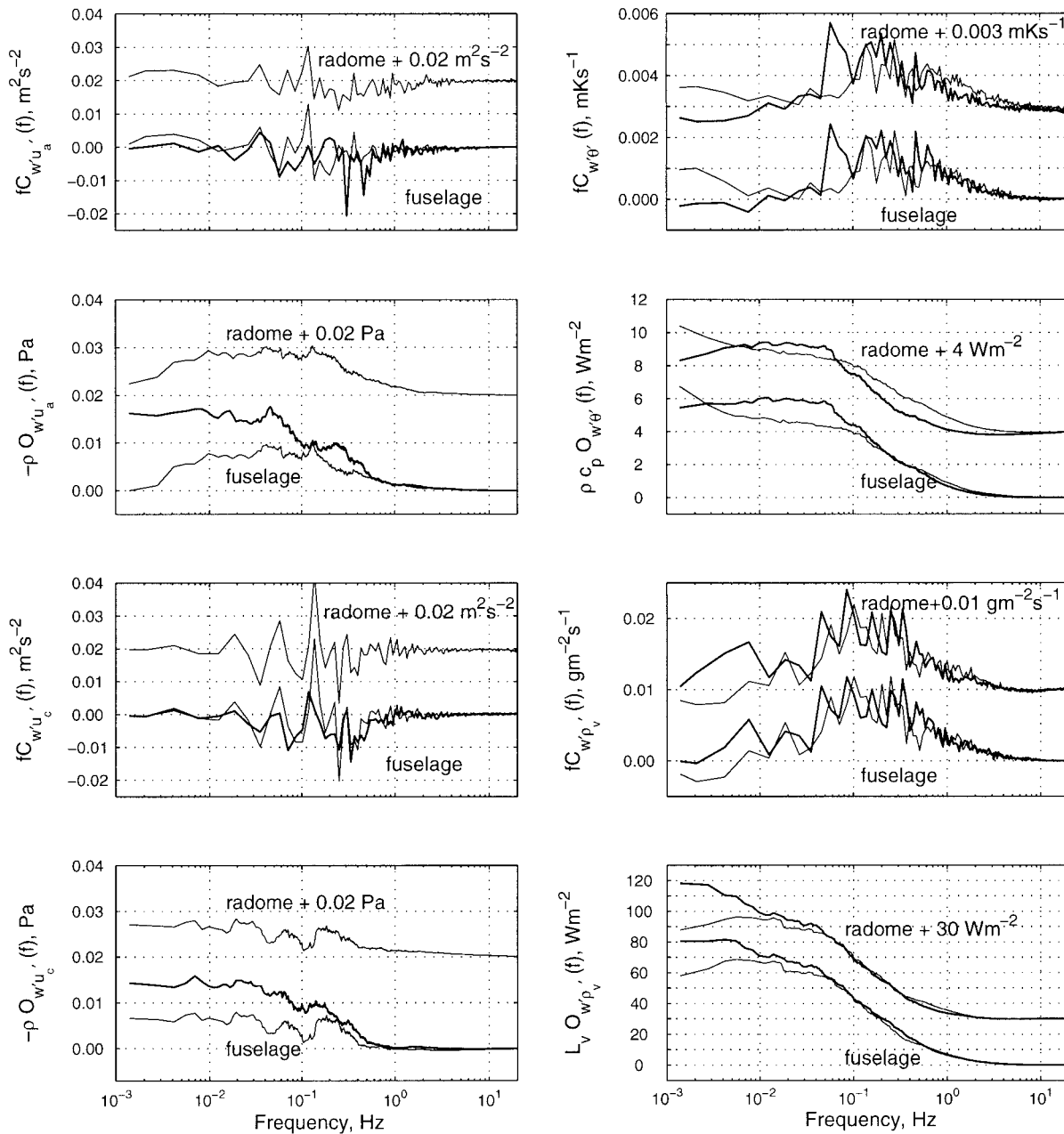


FIG. 7. Cospectra and ogives of along-wind and crosswind momentum fluxes (left) and sensible and latent heat fluxes (right) measured by N42RF (thick line) and N43RF (thin line). As in Fig. 6, radome data were offset deliberately by the amount indicated on each plot for clarity. (Note that  $\theta'$  represents the fluctuations of potential temperature and should not be confused with the pitch angle  $\theta$ .)

angle of attack sensor could have been distorted. This was observed independently of which aircraft was in the lead. However, the variance of  $w$  does not appear to have been affected by whether an aircraft was leading or following (see section 6).

### 6. Results

The two WP-3Ds aircraft were intercompared numerous times in TOGA COARE, especially during the

boundary layer missions. The prevailing light winds and fair weather conditions such as on 28 November 1992 proved to be a good test for the wind measurements. Data shown in this section were obtained after empirical offsets were added to the measured static pressures, ambient and dewpoint temperatures, and dynamic pressures. Except for the latter (see section 4a), the offsets were determined from more comprehensive comparisons with three other aircraft, three ships, and two buoys. These corrective offsets, which were constant

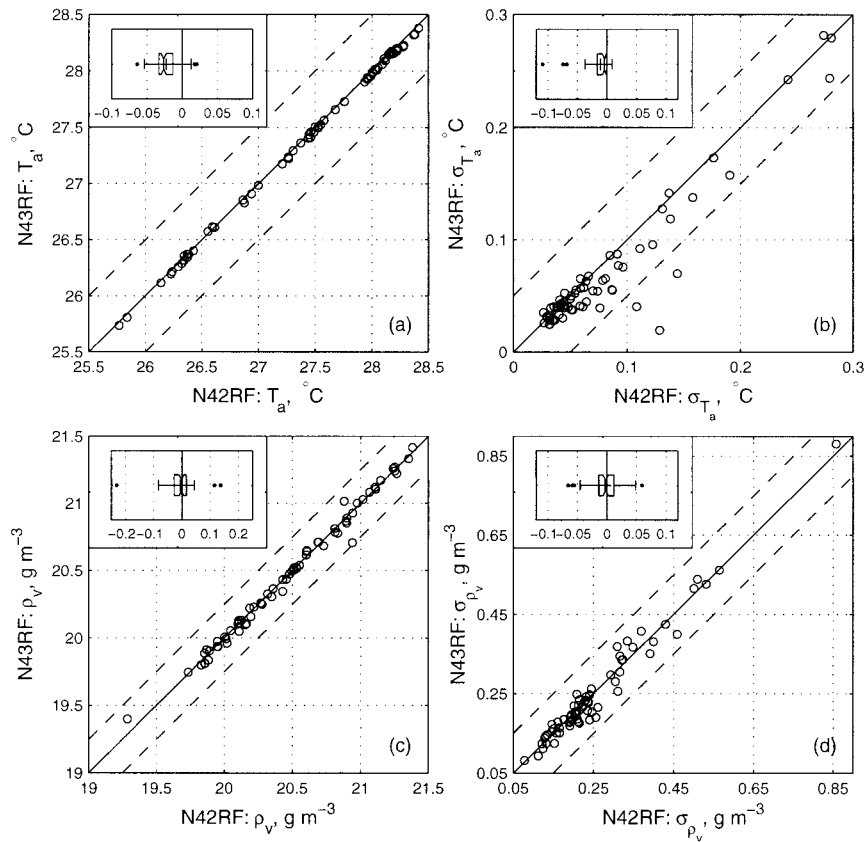


FIG. 8. Comparisons between the two WP-3Ds of means (left) and standard deviations (right) of  $T_a$  (top) and  $\rho_v$  (bottom). Box plots of the N43RF – N42RF differences are given in the inset for each parameter. The units in the box plot are the same as those of the corresponding main plot. Data are from 68 10-km blocks obtained from nine low-level intercomparison runs.

throughout TOGA COARE (except for  $T_a$  on N42RF), are given in Table 2 for the data used in this study.

High-rate (40-Hz) time series and power spectra of wind components, temperature, and absolute humidity measurements from one of these low-level ( $\sim 65$  m) intercomparison legs are shown in Fig. 6. For clarity, the time series have been low-pass filtered at a cutoff frequency of 0.08 Hz. The horizontal wind components from the two aircraft fuselage sensors are in reasonable agreement. Fuselage and radome data are almost identical on N43RF (N42RF radome horizontal winds are excluded because of leaks). The vertical winds also show reasonable agreement. The correlation of  $w$  between radome and fuselage sensors on a given aircraft is good, whereas it is not as good between aircraft because of the lateral separation.

The power spectra of the crosswind component from the two aircraft match closely (Fig. 6), whereas the spectrum of the along-wind velocity on N42RF shows more energy for frequencies above  $\sim 0.25$  Hz. The fuselage vertical wind spectra from the two aircraft are almost identical, differing only at very low frequencies in which  $w$  from N42RF appears to have less spectral energy (comparisons with the NCAR Electra on this same

run, not shown here, confirmed this). The spectrum from N42RF radome vertical wind drops off slightly for frequencies above  $\sim 0.7$  Hz. The time series and power spectra of ambient temperature from the thermistor  $T_a$  and the Lyman- $\alpha$  absolute humidity  $\rho_v$  show reasonable agreement between the two aircraft. Because all power spectra shown in Fig. 6 have been multiplied by  $f^{5/3}$ , the inertial subrange is characterized by a horizontal line. Similar to the findings of Brown et al. (1983), the radome  $w$  data partially resolve the inertial subrange, whereas data from the Rosemount 858Y sensor do not. For the crosswind component, both radome and fuselage data appear to show evidence of the inertial subrange.

The Lyman- $\alpha$  humidity signal has a relatively wide bandwidth (up to 8 Hz), where the inertial subrange may have been captured. The thermistor temperature signal is good up to  $\sim 4$  Hz; for higher frequencies, it is essentially noise for the quiescent conditions of the 921128 flight.

Eddy correlation vertical fluxes of momentum and sensible and latent heats have been calculated for both aircraft. Cospectra and their corresponding ogives (Friehe et al. 1991) of along-wind and crosswind momentum and sensible and latent heats are shown in Fig. 7. The

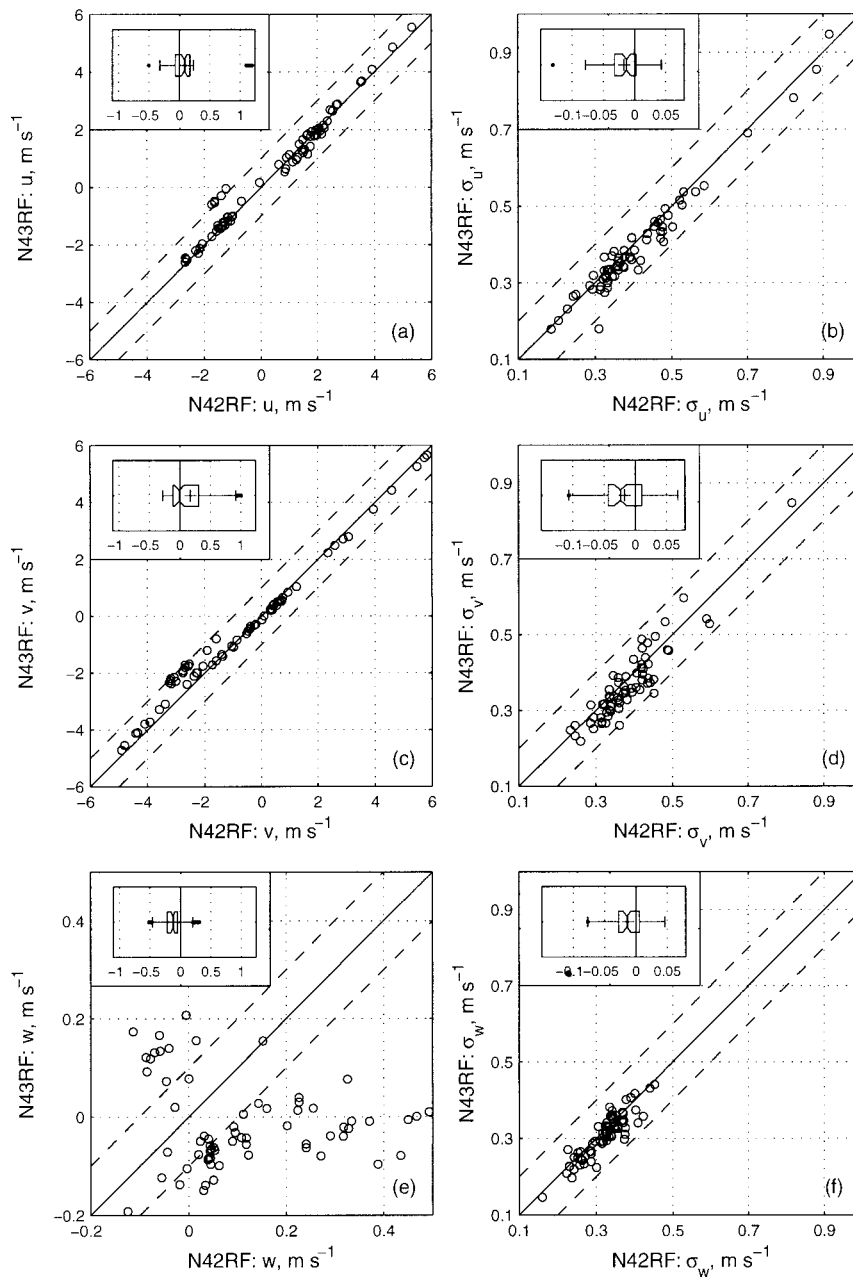


FIG. 9. Comparisons between the two WP-3Ds of means (left) and standard deviations (right) of, from top to bottom,  $u$ ,  $v$ , and  $w$ . Box plots of the N43RF – N42RF differences are given in the insets for each parameter. The units in the box plot are the same as those of the corresponding main plot. Data are from 68 10-km blocks obtained from nine low-level intercomparison runs.

latter two agreed to  $\pm 5\%$ . The momentum fluxes do not agree as well since they are inherently small for the low wind ( $1\text{--}2\text{ m s}^{-1}$ ) conditions.

In order to give an overview of the performance of the two WP-3Ds, a statistical analysis was carried out on nine intercomparison low-level ( $z < 250\text{ m}$ ) runs. Each intercomparison run was divided into 100-s ( $\sim 10\text{ km}$ ) blocks for which means and standard deviations of  $u$ ,  $v$ ,  $w$ ,  $T_a$ , and  $\rho_v$  were compared. Fluxes of latent heat

( $Q_e$ ), sensible heat ( $Q_h$ ), along-wind momentum ( $\tau_a$ ), and crosswind momentum ( $\tau_c$ ) were also compared. Results from 68 blocks are given in Figs. 8–10 as scatterplots and box plots<sup>3</sup>. They are summarized in Table

<sup>3</sup> A box plot (Hoaglin et al. 1983) summarizes data distribution in quartiles, in which the “box” indicates the interquartile range over

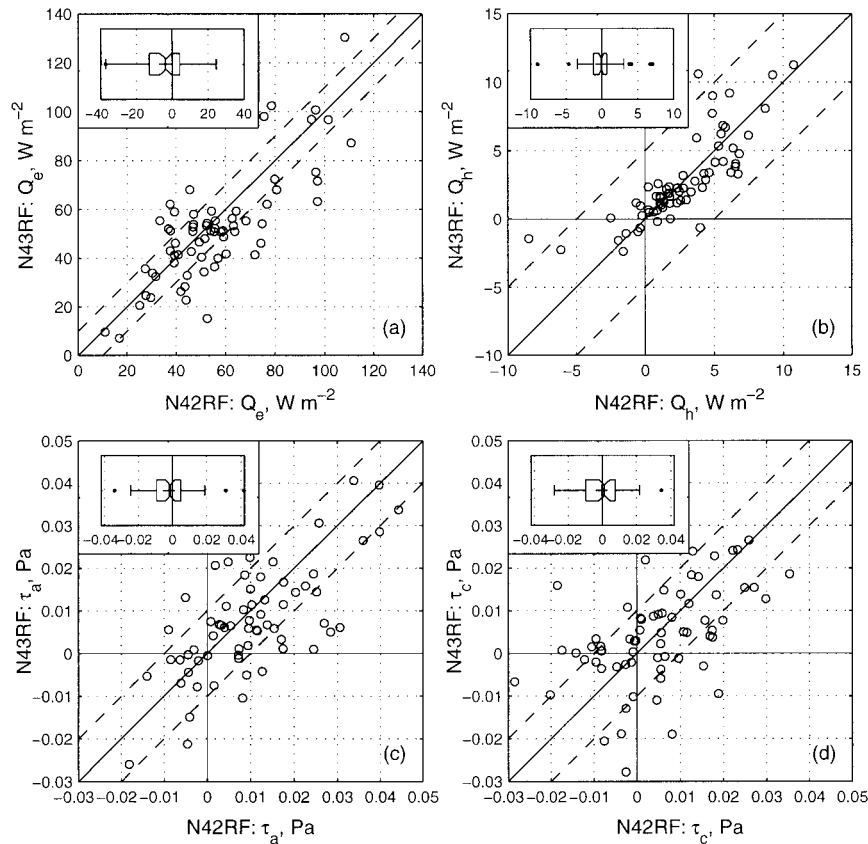


FIG. 10. Flux comparisons between the two WP-3Ds: (a) latent heat flux, (b) sensible heat flux, (c) along-wind stress, and (d) crosswind stress. Box plots of the N43RF – N42RF differences are given in the insets for each flux. The units in the box plot are the same as those of the corresponding main plot. Data are from 68 10-km blocks obtained from nine low-level inter-comparison runs.

3, in which median differences between means and standard deviations of the measurements from the two aircraft were considered rather than mean differences so that the effect of a few outliers is minimized. The deviation about the median was determined as  $\pm 1$  standard deviation.

Discrepancies in  $T_a$  and  $\rho_v$  were found to be smaller than the expected accuracy of the instruments because of the empirical offsets that were added to these scalars prior to their comparison. Differences of mean horizontal wind components from the two aircraft were found to be within  $0.1 \pm 0.4 \text{ m s}^{-1}$ . Means of  $w$  show a large amount of scatter because, as mentioned earlier (section 5b),  $w$  on the trailing aircraft was found to increase by roughly  $0.2 \text{ m s}^{-1}$ . However, there appears

to be no significant difference in the standard deviation of  $w$  between the two aircraft. Figures 10a,b show a reasonable agreement between the two aircraft latent and sensible heat fluxes estimates. Along-wind and crosswind momentum fluxes (Figs. 10c,d) were very small in the predominantly low-wind TOGA COARE conditions and therefore display more scatter. However, they do not seem to have a bias toward either aircraft.

## 7. Discussion and conclusions

Improved aircraft horizontal wind measurements were achieved by (i) using a postflight filtering method to blend the GPS and INS data that removed the approximate  $\pm 1 \text{ m s}^{-1}$  low-frequency errors (caused by Schuler oscillation and drift) and the approximate  $\pm 0.5 \text{ m s}^{-1}$  high-frequency oscillations from INS-measured ground-speed components of the aircraft, and (ii) incorporating moist-air thermodynamic properties in the calculation of true airspeed that was found to be  $\sim 0.6 \text{ m s}^{-1}$  larger than that calculated for dry air for typical tropical conditions.

Horizontal winds from the two WP-3Ds agreed within

which the middle 50% of the data are distributed. The lowest 25% of the data are between the lower end of the box and the lowest whisker end point, and the upper 25% is between the upper end of the box and the upper end of the whisker. The line through the box shows the median, + shows the mean, and ● show outliers of differences between measurements from the two aircraft.

TABLE 3. Median differences between means and standard deviations of ambient temperature, absolute humidity ( $l_v$ ) and wind components measurements, and median differences between latent and sensible heat and momentum flux measurements from the two WP-3D aircraft. Deviation about the median was determined as  $\pm 1$  standard deviation. Results are from 68 10-km blocks obtained from nine low-level intercomparison runs.

N43RF-N42RF	$T_a$ (°C)	$l_v$ (g m <sup>-3</sup> )	$u$ (m s <sup>-1</sup> )	$v$ (m s <sup>-1</sup> )	$w$ (m s <sup>-1</sup> )	$Q_e$ (W m <sup>-2</sup> )	$Q_h$ (W m <sup>-2</sup> )	$\tau_a$ (Pa)	$\tau_c$ (Pa)
Mean	$-0.03 \pm 0.02$	$0 \pm 0.05$	$0.1 \pm 0.4$	$0 \pm 0.4$	$-0.1 \pm 0.2$	$-3.5 \pm 14$	$0 \pm 2.5$	$0 \pm 0.015$	$0 \pm 0.015$
Standard deviation	$0 \pm 0.02$	$0 \pm 0.03$	$0 \pm 0.03$	$-0.02 \pm 0.04$	$0 \pm 0.03$				

$\pm 0.4$  m s<sup>-1</sup>. The main source of remaining uncertainty on  $u$  and  $v$  is, we believe, the heading. Differences in headings from two INS on the same aircraft were about  $\pm 0.2^\circ$  for most flights. [Lenschow (1986) estimated that for an aircraft speed of 100 m s<sup>-1</sup>, a  $0.3^\circ$  error in heading would induce a  $0.5$  m s<sup>-1</sup> error in the mean wind.] Use of modern INS units combined with multiple antenna GPS should ameliorate the heading measurements and thus improve further the accuracy of  $u$  and  $v$ . An alternative method would be to use a Kalman filter technique to integrate INS data with GPS data to achieve an approximate  $\pm 0.02^\circ$  heading accuracy (Leach and MacPherson 1994).

A digital filtering method was used to determine an accurate 1-Hz aircraft vertical velocity from the INS vertical acceleration and pressure altitude signals to avoid the time lag introduced by the baro-inertial loop method. A novel method that minimized both mean and variance of  $w$  on a large collection of low-level-run data from several flights was developed to determine the slope and offset of the radome and fuselage angle of attack calibration.

Spectra of wind components from the two aircraft were in reasonable agreement. It was also found that the radome system had a response to  $\sim 9$  Hz (just starting to resolve the inertial subrange); the Rosemount 858Y fuselage system response was good to only  $\sim 4$  Hz. However, fluxes measured using data from the latter were comparable with those determined from the radome winds, which indicates that its response is good enough to resolve most flux-carrying eddies.

An estimate of the the NOAA WP-3Ds measurements overall accuracy was obtained from in situ comparisons between the two aircraft during TOGA COARE. Mean differences of  $u$ ,  $v$ , and  $w$  between the two aircraft were found close to zero, and the scatter was within the accuracy of instrumentation, as summarized in Table 3. It was also found that the standard deviations of these parameters were practically the same on the two aircraft. Differences in latent and sensible heat fluxes and momentum flux components between the two aircraft were  $3.5 \pm 15$  W m<sup>-2</sup>,  $0 \pm 2.5$  W m<sup>-2</sup>, and  $0 \pm 0.015$  Pa, respectively.

*Acknowledgments.* We acknowledge NOAA-AOC flight crews and engineers for their cooperation, especially Barry Damiano, who always fulfilled our requests. Ed Brown of NCAR and Barry Damiano performed the

trailing cone flights. The optimization method for angle of attack calibration was the idea of Perry Fuehrer. We also acknowledge Ed Brown, Timothy Crawford, Barrie Leach, and Yolande Serra for their thoughtful reviews, and Xilong Song and Bryan Hannegan for their invaluable comments. This work was supported by National Science Foundation Grants ATM-9024436 and ATM-9110540 and NOAA Grant 56GP0154-01.

## APPENDIX

### Moist Airspeed Equations

The use of moist-air thermodynamic properties in the compressible flow equations is required when conditions of high humidity and low winds prevail. An analysis similar to that of Iribarne and Godson (1981) was used to derive the moist-air thermodynamic properties and is developed further in this appendix.

The heat  $\delta Q_p$  absorbed at constant pressure by a moist-air parcel with mass  $m$  and specific humidity  $q$  for an increase  $dT$  in its temperature is

$$\delta Q_p = m_d \delta q_d + m_v \delta q_v = [(1 - q) \delta q_d + q \delta q_v] m, \quad (A1)$$

where  $m_d$  and  $m_v$  are the mass of dry air and water vapor and  $\delta q_d$  and  $\delta q_v$  are the heats absorbed by unit mass of dry air and of water vapor, respectively. Dividing by  $m dT$  and rearranging,

$$c_p = c_{pd} \left[ 1 + q \left( \frac{c_{pv}}{c_{pd}} - 1 \right) \right], \quad (A2)$$

where  $c_p$ ,  $c_{pd}$ , and  $c_{pv}$  are the specific heats at constant pressure for moist air, dry air, and water vapor, respectively. The same reasoning can be made when considering the heat  $\delta Q_v$  absorbed at constant volume for an increase  $dT$  in temperature, which leads to

$$c_v = c_{vd} \left[ 1 + q \left( \frac{c_{vv}}{c_{vd}} - 1 \right) \right], \quad (A3)$$

where  $c_v$ ,  $c_{vd}$ , and  $c_{vv}$  are the specific heats at constant volume for moist air, dry air, and water vapor, respectively.

Because dry air is mainly a diatomic gas and water vapor is a triatomic nonlinear molecule,

$$c_{vd} = \frac{5}{2}R_d \quad (\text{A4})$$

$$c_{pd} = \frac{7}{2}R_d \quad (\text{A5})$$

$$c_{vv} = 3R_v \quad (\text{A6})$$

$$c_{pv} = 4R_v, \quad (\text{A7})$$

where  $R_d$  and  $R_v$  are the gas constants of water vapor and dry air. Substituting Eqs. (A5) and (A7) into Eq. (A2) and substituting Eqs. (A4) and (A6) into Eq. (A3),

$$c_p = c_{pd} \left[ 1 + q \left( \frac{8}{7\epsilon} - 1 \right) \right] \quad (\text{A8})$$

$$c_v = c_{vd} \left[ 1 + q \left( \frac{6}{5\epsilon} - 1 \right) \right], \quad (\text{A9})$$

where  $\epsilon$  is the ratio of molecular weight of water vapor to that of dry air. The moist-air gas “constant”  $R$ , which is no longer a constant, since it varies with humidity, is obtained by taking the difference between Eqs. (A8) and (A9):

$$R = c_p - c_v = R_d \left( 1 - q + \frac{q}{\epsilon} \right). \quad (\text{A10})$$

The ratio of specific heats  $\gamma$  of moist air is obtained by taking the ratio of Eqs. (A8) and (A9) after replacing  $q$  with  $r/(1+r)$ , where  $r$  is the mixing ratio

$$\gamma = \gamma_d \left[ 1 - \frac{2}{7} \frac{r}{5\epsilon + 6r} \right]. \quad (\text{A11})$$

Equations (A8), (A9), (A10), and (A11) show that, compared with dry air, moist air has greater specific heats and gas constant but a smaller specific heat ratio. These expressions require the measurement of a humidity parameter such as specific humidity or mixing ratio. One way to obtain these is to measure the dewpoint and then to determine the partial water vapor pressure using the Goff–Gratch formulation with the “enhancement factor” (to account for the fact that moist air is considered and not pure water) as in Buck (1981) and Miller and Friesen (1989). These formulae are summarized below.

The water vapor pressure over a plane water surface ( $T_a \geq 273.15$  K)  $e_w$  is given by the expression of its decimal logarithm (for clarity):

$$\begin{aligned} \log_{10} e_w = & 23.832\,241 - 5.028\,08 \log_{10} T \\ & - 1.3816 \times 10^{-7} \times 10^A \\ & + 8.1328 \times 10^{-3} \times 10^B + C, \end{aligned} \quad (\text{A12})$$

where

$$A = 11.334 - 0.030\,399\,8T, \quad (\text{A13})$$

$$B = 3.491\,49 - 1302.8844T^{-1}, \quad (\text{A14})$$

$$C = -2949.076T^{-1}, \quad (\text{A15})$$

and similarly, the water vapor pressure over a plane ice surface ( $T_a < 273.15$  K)  $e_i$  is given by the expression of its decimal logarithm

$$\begin{aligned} \log_{10} e_i = & 3.566\,54 \log_{10} T - 0.003\,209\,8T \\ & - 2484.956T^{-1} + 2.070\,229\,4. \end{aligned} \quad (\text{A16})$$

Equations (A12) and (A16) yield the saturated water vapor pressure when  $T$  is the ambient temperature  $T_a$ , and yield the nonsaturated water vapor pressure when  $T$  is the dewpoint temperature  $T_d$  ( $T$  in kelvins). Since it is moist air and not pure water that is involved, enhancement factors  $f_w$  and  $f_i$  are introduced to correct the estimated water vapor pressures (Buck 1981). The corrected pressures are

$$e_{wc} = f_w e_w \quad (\text{A17})$$

$$e_{ic} = f_i e_i, \quad (\text{A18})$$

where

$$f_w = 1.0007 + 3.46 \times 10^{-6} P_s \quad (\text{A19})$$

$$f_i = 1.0003 + 4.18 \times 10^{-6} P_s \quad (\text{A20})$$

and  $P_s$  is the static pressure expressed in hPa. The water vapor pressure  $e_v$  obtained from Eqs. (A12) and (A16) (with  $T = T_d$ ) is used to calculate  $q$  and  $r$ :

$$r = \epsilon \frac{e_v}{P_s - e_v} \quad (\text{A21})$$

$$q = \epsilon \frac{e_v}{P_s + (\epsilon - 1)e_v}. \quad (\text{A22})$$

The method used to derive ambient temperature  $T_a$  and true airspeed  $U_a$  is the same as that of Lenschow and Spyers-Duran (1989) except that their correction of true airspeed for humidity effects is overestimated, based on the early work of Friehe, and Lenschow and Spyers-Duran (1989) do not account for the Mach number dependence of the recovery factor. The equation of  $T_a$  and  $U_a$  can be found in Lenschow (1986):

$$T_a = \frac{T_r}{R_f M^2 \left( \frac{\gamma - 1}{2} \right) + 1} \quad (\text{A23})$$

and

$$U_a = \left[ \frac{\gamma R T_r}{R_f \left( \frac{\gamma - 1}{2} \right) + \frac{1}{M^2}} \right]^{1/2}, \quad (\text{A24})$$

where  $T_r$  is the recovery temperature,  $R_f$  is the total temperature probe recovery factor, and  $M$  is the Mach number.

To give an estimate of the humidity effects on true airspeed, WP-3D data from a large number of soundings were considered. The ratio of true airspeeds calculated

using moist- and dry-air properties was first-order least squares fit to specific humidity (which varied in the range of 1–20 g kg<sup>-1</sup>) to give

$$\frac{U_{am}}{U_{ad}} = 0.000304q + 1, \quad (\text{A25})$$

where  $U_{am}$  and  $U_{ad}$  are the “moist” and “dry” true airspeeds, respectively, and  $q$  is the specific humidity in g kg<sup>-1</sup>. For  $q = 18$  g kg<sup>-1</sup>, the true airspeed will increase by 0.55% from that obtained for dry air. For the  $\sim 110$  m s<sup>-1</sup> average WP-3Ds true airspeed during the low-level boundary-layer runs, this would correspond to a 0.6 m s<sup>-1</sup> net increase in true airspeed. If not accounted for, these humidity effects would represent a significant error for the low winds (approximately 2–4 m s<sup>-1</sup>) that prevailed in TOGA COARE.

#### REFERENCES

- Axford, D. N., 1968: On the accuracy of wind measurements using an inertial platform in an aircraft, and an example of a measurement of the vertical mesostructure of the atmosphere. *J. Appl. Meteor.*, **7**, 645–666.
- Blanchard, R. L., 1971: A new algorithm for computing inertial altitude and vertical velocity. *IEEE Trans. Aerosp. Electron. Syst.*, **AES-7**, 1143–1146.
- Bögel, W., and R. Baumann, 1991: Test and calibration of the DLR Falcon wind measuring system by maneuvers. *J. Atmos. Oceanic Technol.*, **8**, 5–18.
- Brown, E. N., 1988: Position error calibration of a pressure survey aircraft using a trailing cone. NCAR/TN-313+STR, 29 pp. [Available from NCAR, P.O. Box 3000, Boulder, CO 80307.]
- , C. A. Friehe, and D. H. Lenschow, 1983: The use of pressure fluctuations on the nose of an aircraft for measuring air motion. *J. Climate Appl. Meteor.*, **22**, 171–180.
- Buck, A. L., 1981: New equations for computing vapor pressure and enhancement factor. *J. Appl. Meteor.*, **20**, 1527–1532.
- Friehe, C. A., and D. Khelif, 1992: Fast-response aircraft temperature sensors. *J. Atmos. Oceanic Technol.*, **9**, 784–795.
- , R. L. Grossman, and Y. Pann, 1986: Calibration of an airborne lyman-alpha hygrometer and measurement of water vapor flux using a thermoelectric hygrometer. *J. Atmos. Oceanic Technol.*, **3**, 299–304.
- , and Coauthors, 1991: Air–sea fluxes and surface-layer turbulence around a sea surface temperature front. *J. Geophys. Res.*, **96** (C5), 8593–8609.
- , S. P. Burns, D. Khelif, and X. Song, 1996: Meteorological and flux measurements from the NOAA WP-3D aircraft in TOGA COARE. Preprints, *Eighth Conf. on Air–Sea Interaction and Conf. on the Global Ocean–Atmosphere–Land System (GOALS)*, Atlanta, GA, Amer. Meteor. Soc., J42–J45.
- Fuehrer, P. L., C. A. Friehe, and D. K. Edwards, 1994: Frequency response of a thermistor temperature probe in air. *J. Atmos. Oceanic Technol.*, **11**, 476–488.
- Hoaglin, D. C., F. Mosteller, and J. W. Tukey, 1983: *Understanding Robust and Exploratory Data Analysis*. Wiley, 447 pp.
- Iribarne, J. V., and W. L. Godson, 1981: *Atmospheric Thermodynamics*. D. Reidel, 259 pp.
- Leach, B. W., and J. I. MacPherson, 1991: An application of Kalman filtering to airborne wind measurement. *J. Atmos. Oceanic Technol.*, **8**, 51–65.
- , and —, 1994: Comments on “Correction of inertial navigation with Loran C on NOAA’s P-3 aircraft.” *J. Atmos. Oceanic Technol.*, **11**, 1048–1053.
- LeMone, M. A., and W. T. Pennell, 1980: A comparison of turbulence measurements from aircraft. *J. Appl. Meteor.*, **19**, 1420–1437.
- Lenschow, D. H., 1986: Aircraft measurements in the boundary layer. *Probing the Atmospheric Boundary Layer*, D. H. Lenschow, Ed., Amer. Meteor. Soc., 39–55.
- , and P. Spysers-Duran, 1989: Measurement techniques: Air motion sensing. NCAR Research Aviation Facility Bull. 23, 36 pp. [Available from NCAR, P.O. Box 3000, Boulder, CO 80307.]
- , E. R. Miller, and R. B. Friesen, 1991: A three-aircraft intercomparison of two types of air motion measurement systems. *J. Atmos. Oceanic Technol.*, **8**, 41–50.
- Liepmann, H. W., and A. Roshko, 1967: *Elements of Gasdynamics*. J. Wiley & Sons, 439 pp.
- MacPherson, J. I., R. L. Grossman, and R. D. Kelly, 1992: Intercomparison results for FIFE flux aircraft. *J. Geophys. Res.*, **97** (D17), 18 499–18 514.
- Masters, J. M., and J. A. Leise, 1993: Correction of inertial navigation with LORAN C and NOAA’s P-3 aircraft. *J. Atmos. Oceanic Technol.*, **10**, 145–154.
- Matejka, T., and S. A. Lewis, 1997: Improving research aircraft navigation by incorporating INS and GPS information in a variational solution. *J. Atmos. Oceanic Technol.*, **14**, 495–511.
- Miller, E. R., and R. B. Friesen, 1989: Standard output data products from the NCAR research aviation facility. NCAR Research Aviation Facility Bull., **9**, 64 pp.
- Rosemount, 1981: Total temperature sensors. Rosemount Engineering Company Tech. Bull. 5755, Rev. A, 28 pp. [Available from Rosemount Eng. Co., P.O. Box 35129, Minneapolis, MN 55435.]
- Tjernstrom, M. T., and C. A. Friehe, 1991: Analysis of a radome air motion system on a twin-jet-aircraft for boundary layer research. *J. Atmos. Oceanic Technol.*, **8**, 19–40.
- , and P. Samuelsson, 1995: The effect of inertial navigation system time response on airborne turbulence measurements. *J. Atmos. Oceanic Technol.*, **12**, 1196–1213.
- Webster, P. J., and R. Lukas, 1992: TOGA COARE: The coupled ocean–atmosphere response experiment. *Bull. Amer. Meteor. Soc.*, **73**, 1377–1416.
- Wood, R., I. M. Stromberg, P. R. Jonas, and C. S. Mill, 1997: Analysis of an air motion system on a light aircraft for boundary layer research. *J. Atmos. Oceanic Technol.*, **14**, 960–968.